Nano Energy 52 (2018) 29–37

Contents lists available at ScienceDirect

Nano Energy

journal homepage: www.elsevier.com/locate/nanoen

Full paper

Well-elaborated, mechanochemically synthesized Fe-TPP ⊂ ZIF precursors (Fe-TPP = tetraphenylporphine iron) to atomically dispersed iron–nitrogen species for oxygen reduction reaction and Zn-air batteries

Wei Wei[a,*], Xiaomeng Shi[a], Peng Gao[a], Shanshan Wang[b], Wei Hu[d], Xiaoxiao Zhao[b], Yuanman Ni[b], Xiaoyan Xu[a], Yanqing Xu[b], Wensheng Yan[d], Hengxing Ji[c,*], Minhua Cao[b,*]

[a] Department of Chemistry, Capital Normal University, Beijing 100048, PR China
[b] Laboratory of Cluster Science, Ministry of Education of China, Beijing Key Laboratory of Photoelectronic/Electrophotonic Conversion Materials, School of Chemistry and Chemical Engineering, Beijing Institute of Technology, Beijing 100081, PR China
[c] Department of Materials Science and Engineering, CAS Key Laboratory of Materials for Energy Conversion, iChEM, University of Science and Technology of China, Hefei, Anhui 230029, PR China
[d] National Synchrotron Radiation Laboratory, University of Science and Technology of China, Hefei, Anhui 230029, PR China

ARTICLE INFO

Keywords:
Mechanochemical synthesis
Host-guest complexes
Iron-nitrogen-doped carbon
Single-atom catalyst
Oxygen reduction reaction

ABSTRACT

Although atomically dispersed Fe-N species as electrocatalysts often exhibit high activity for oxygen reduction reaction (ORR), the rational design and facile fabrication of single-atom Fe-N species-based catalysts remains a great challenge because of their easy aggregation. Herein, a new precursor of host-guest Fe-TPP ⊂ *rho*-ZIF (Fe-TPP = tetraphenylporphyrin iron; *rho*-ZIF = zeolitic imidazolate framework with the *rho* topology) for the first time was elaborately designed and readily prepared by one-pot mechanochemical method, and then was pyrolyzed into Fe-N/C catalysts with no need of solution-based steps and post-ammonia/acid treatments, which greatly simplified the preparation procedures. Owing to the host-guest confinement at the molecular level, the encapsulated Fe centers within interior cavities of *rho*-ZIF host matrice can be effectively isolated during pyrolysis to afford atomically dispersed Fe-N_4 moieties anchored on the carbon matrice. Such a well-elaborated precursor not only endows the final product with the single-atom characteristic, but also with high Fe loading (up to 3.8 wt%) and specific surface area. Benefitting from the outstanding compositional and structural advantages, the resultant Fe-N/C exhibits highly efficient ORR activity with $E_{1/2}$ of 0.895 V in 0.1 M KOH, ~ 50 mV more positive than that of the commercial Pt/C, which is among the top-level ORR electrocatalysts to date. It has excellent stability and displays a negligible change after a 10000-cycle accelerated durability test. Moreover, rechargeable Zn-air batteries were also assembled to demonstrate the practical application of the as-obtained Fe-N/C as air cathode catalyst. Our work may provide an insight into the facile and large-scale production of high-performance and durable non-precious metal catalysts with atomic-level dispersion.

1. Introduction

The electrochemical oxygen reduction reaction (ORR) has attracted extensive interest owing to its importance in renewable and sustainable energy systems, such as metal-air batteries and fuel cells [1–6]. The high cost of the widely used Pt-based catalysts is a key obstacle for their large-scale application [7–9]. As one of the most promising substitutes, iron and nitrogen codoped carbon (Fe-N/C) catalysts exhibit super ORR activity, and the atomically dispersed Fe-N_x moieties in carbon matrix are considered to be important active sites for the ORR electrocatalysis process, which has been well addressed by many studies [10–13]. Nevertheless, the most commonly used synthesis process of Fe-N/C involves a physical mixing of C, N and Fe precursors followed by an annealing treatment, and some Fe-based byproducts (such as FeN_x, Fe, Fe_3C) would also be formed inevitably [14–18], thereby leading to a low utilization of the Fe precursors and a low dispersion density of active Fe-N_x moieties [19]. Thus, the scrupulous design of the precursor to realize accurate fabrication of Fe single-atom catalysts (SACs) becomes particularly important for maximizing the iron atom efficiency and achieving high catalytic performance [20–24]. Although much effort has been devoted to effectively dispersing and isolating single-atom centers, it is still a great challenge to avoid their easy migration and

* Corresponding authors.
E-mail addresses: wwei@cnu.edu.cn (W. Wei), jihengx@ustc.edu.cn (H. Ji), caomh@bit.edu.cn (M. Cao).

https://doi.org/10.1016/j.nanoen.2018.07.033
Received 25 April 2018; Received in revised form 29 June 2018; Accepted 15 July 2018
Available online 17 July 2018
2211-2855/

agglomeration in the synthesis process of SACs [25–27]. In addition, some fabrication processes usually include many tedious procedures such as solution-based synthesis of the precursors [28–31], acid washing [15,32–34], and ammonia post-treatment [28,35,36], which not only produce environmentally harmful waste but also prolong the preparation process. To overcome these problems, a suitable precursor system that can effectively isolate and anchor Fe-N centers, is highly needed for achieving time-saving, environmentally friendly synthesis of atomically dispersed Fe-N/C catalysts with high utilization efficiency of the iron atoms as well as high electrocatalytic activity [31].

Mechanochemistry is featured as a fast, energy efficient and eco-friendly high-yield methodology for promoting reactions between solids [37,38]. Friščić and co-workers have developed some improved mechanochemical approaches for the facile preparation of a number of metal-organic frameworks (MOFs) [39–42]. As we know, the conventional solution-based methods used to prepare MOFs often suffer from typical low-yield and time-consuming issues, greatly limiting their practical applications, whereas the mechanochemical approach can achieve macroscale and facile preparation of MOFs. Among various MOFs, zeolitic imidazolate frameworks (ZIFs) [43], owing to the large interior cages and relatively small windows, are extremely attractive as host matrice for encapsulating and immobilizing large guest molecules [44–46]. With the efficient non-solution synthesis approach of ZIFs in hand, we wish to be able to encapsulate metalloporphyrin complexes into the interior cavities of ZIFs by *in-situ* host–guest nanoconfinement to form molecular-level integrated precursors (metalloporphyrin⊂ZIFs). There might be several remarkable advantages for employing such host-guest metalloporphyrin⊂ZIF complexes as the precursor to prepare Fe-N/C catalysts: (i) Porphyrin architectures contain a high number of nitrogen species, four pyrrolic nitrogen sites, which could act as the anchoring points to strongly stabilize single-atom metals for effective promotion of ORR [47–49]. (ii) Different from uncertain and uncontrollable configurations of Fe centers by direct pyrolysis of iron macrocycle complexes [50–52], the confinement effect of the well-defined cavities of ZIFs could ensure the uniform dispersion and effective isolation of the definite Fe-N_4 centers, preventing the aggregation of Fe atoms during the annealing process and accordingly improving the utilization efficiency of iron atoms. (iii) During the high-temperature pyrolyzation process, the sublimed Zn species from ZIFs would lead to the formation of abundant channels in final Fe-N/C product, which is beneficial for the diffusion of reactive species and the exposure of the Fe-N_x active sites, thus further promoting the electrocatalytic properties [31,53–60].

Herein, we for the first time demonstrate the encapsulation of large tetraphenylporphyrin iron (Fe-TPP) molecules into the large interior cages of *rho*-ZIF (a kind of ZIF with the *rho* topology) by high-yield mechanochemical method to form the host-guest Fe-TPP⊂*rho*-ZIF complexes, which then serve as the precursor experiencing pyrolyzation to form an atomically dispersed Fe-N/C catalyst with the single-atom Fe loading as high as 3.8 wt%. Such a high Fe loading is closely related to the well-elaborated design of the Fe-TPP⊂*rho*-ZIF precursor, which can realize the effective isolation of single-iron centers due to the host-guest confinement. In addition, the whole synthesis process did not involve any solution-based steps and post-ammonia/acid treatments, which greatly simplified the preparation procedures of Fe-N/C catalysts. The as-obtained catalyst exhibited highly efficient ORR activity with high $E_{1/2}$ of 0.895 V in 0.1 M KOH, which is ~ 50 mV more positive than that of the commercial Pt/C. Additionally, Fe-N/C shows good methanol tolerance and excellent stability, displaying no obvious current change in the presence of 3.0 M methanol or a 10000-cycle accelerated durability test. Moreover, rechargeable Zn-air batteries were also assembled using Fe-N/C as air cathode to demonstrate its practical application.

2. Experimental

2.1. Preparation of materials

2.1.1. Preparation of Fe-TPP⊂rho-ZIF

Synthetic reactions were performed in an 80 mL zirconia milling pot with 10 mm diameter zirconia balls. 1 mmol of ZnO, 3 mmol of 2-ethylimidazole, 0.0756 mmol of $(NH_4)_2SO_4$ (~10 mg) and various amounts of Fe-TPP (molar ratios of Fe-TPP/ZnO are 1/20, 1/30 and 1/40, respectively) were put into the pot with adding 200 μL of N,N-diethylformamide (DEF), and then the resultant mixture was milled for 2 × 30 min at 50 Hz to afford a large number of dark green solids, *i.e.*, Fe-TPP⊂*rho*-ZIF-1/20, Fe-TPP⊂*rho*-ZIF-1/30 and Fe-TPP⊂*rho*-ZIF-1/40.

2.1.2. Preparation of Fe-N/C catalysts

The powders of Fe-TPP⊂*rho*-ZIF precursors were pyrolyzed in a tube furnace using a programmed heating process at 950 °C for 3 h under N_2 atmosphere with a heating rate of 2 °C min^{-1}. Fe-C/N catalysts were obtained when the tube furnace was cooled to ambient temperature naturally, and they are denoted as Fe-N/C-1/20, Fe-N/C-1/30, and Fe-N/C-1/40, respectively. If *rho*-ZIF was directly pyrolyzed with same reaction conditions, N-doped carbon (denoted as N/C) was obtained.

2.1.3. Preparation of Fe-N/C-mix

1 mmol of ZnO, 3 mmol of 2-ethylimidazole, 0.0756 mmol of $(NH_4)_2SO_4$ (~ 10 mg) and 200 μL of DEF were put into the zirconia pot and ground for 2 × 30 min at 50 Hz to afford pristine *rho*-ZIF. Then, the as-synthesized pristine rho-ZIF and 1/30 mmol Fe-TPP were mixed and ground for 5 min, and the mixed solid was pyrolyzed at 950 °C for 3 h under N_2 atmosphere to afford Fe-N/C-mix.

2.2. Characterizations

The size and morphology of the products were characterized by a JEOL JEM100-CXII transmission electron microscope (TEM). The high-angle annular dark-field scanning transmission electron microscopy (HAADF-STEM) and corresponding energy-dispersive spectroscopy (EDS) mapping analyses were executed on a JEOL JEM-ARF200F TEM/STEM with a spherical aberration corrector. The structure of samples was performed on a Bruker D8 Focus X-ray powder diffractometer (XRD) with Cu Kα radiation (λ = 1.5406 Å). The nitrogen adsorption/desorption isotherms and corresponding pore size distribution were measured using a Micromeritics ASAP 2020 system at 77 K. X-ray photoelectron spectroscopy (XPS) measurements were performed on Thermo escalab 250Xi using Al Kα irradiation. Raman spectra were performed using an Renishaw inVia Raman spectrometer with an excitation laser wavelength of 532 nm.

The absorption spectra of Fe K-edge were collected in transmission mode using a Si (111) double-crystal monochromator at the X-ray absorption fine structure (XAFS) station of the BL11U beamline of national synchrotron radiation laboratory (NSRL, Hefei). The storage rings of NSRL was operated at 0.8 GeV with a maximum current of 300 mA. The data collection was carried out in transmission mode using ionization chamber for Fe foil, Fe_2O_3, and in fluorescence excitation mode using a Lytle detector for Fe-N/C-1/30. All spectra were collected in ambient conditions.

The acquired extended X-ray absorption fine structure (EXAFS) data were extracted and processed according to the standard procedures using the ATHENA module implemented in the IFEFFIT software packages [61]. The k^3-weighted EXAFS spectra were obtained by subtracting the post-edge background from the overall absorption and then normalizing with respect to the edge-jump step. Subsequently, k^3-weighted χ(k) data in the k-space were Fourier transformed to real (R) space using a hanning windows (d_K = 1.0 $Å^{-1}$) to separate the EXAFS

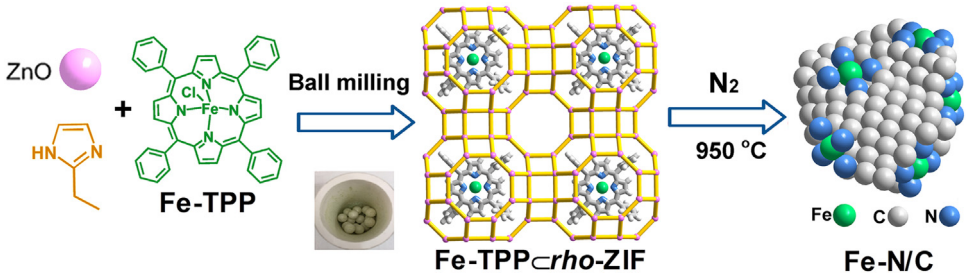

Scheme 1. The schematic illustration for the non-solution fabrication process of Fe-N/C.

contributions from different coordination shells.

2.3. Electrochemical measurements

2.3.1. Electrode preparation and ORR tests

All the electrochemical measurements were carried out in a conventional three-electrode system on a CHI760E electrochemical station. A rotating disk electrode (RDE) with a glassy carbon (GC) disk (5 mm in diameter) and a rotating ring-disk electrode (RRDE) with a Pt ring (8.5 mm outer diameter and 6.5 mm inner diameter) and a glassy carbon (GC) disk (5.5 mm diameter) were used as the substrate for the working electrode. Ag/AgCl (KCl, saturated) and a platinum foil (1 cm^2) were used as reference and counter electrodes, respectively. 4 mg of catalyst was dispersed in 1 mL of solution containing ethanol and 5 wt% Nafion with the volume ratio of 9:1, and then sonicated for 1 h to form a homogeneous catalyst ink. Then 20 μL of the catalyst ink was loaded onto the GC electrode, which was dried at ambient temperature for electrochemical measurements. For comparison, a commercial Pt/C catalyst (20 wt% platinum in carbon) with the same amount was also studied. Before tests, Ar/O_2 flow was bubbled into the cell for about 30 min to achieve the Ar/O_2-saturated solution. The electrochemical experiments were carried out in O_2-saturated 0.1 M KOH and 0.5 M H_2SO_4 electrolytes for ORR, respectively. The cyclic voltammetry (CV) tests were measured with a scan rate of 50 mV s^{-1}. ORR and RDE measurements were performed at various rotating speeds from 400 to 1600 rpm at a scan rate of 10 mV s^{-1}. The electron transfer number (n) were determined by the Koutecky-Levich equation:

$$\frac{1}{J} = \frac{1}{J_k} + \frac{1}{\left(B\omega^{\frac{1}{2}}\right)} \quad (1)$$

$$B = 0.2nFC_0D_0^{\frac{2}{3}}\nu^{\frac{-1}{6}} \quad (2)$$

$$J_k = nFkC_0 \quad (3)$$

where J is the measured current density, J_K is the kinetic current density, ω is the angular velocity of the disk, n is the overall number of electrons transferred in oxygen reduction, F is the Faraday constant (96485 C mol^{-1}), C_0 is the bulk concentration of O_2 (1.21×10^{-6} mol cm^{-3}), D_0 is the diffusion coefficient of O_2 in 0.1 M KOH (1.9×10^{-5} cm^2 s^{-1}), v is the kinematic viscosity of the electrolyte (0.01 cm^2 s^{-1}), and k is the electron transfer rate constant.

The yield of HO_2^- and the electron transfer number (n) from RRDE measurements were calculated with the following equations:

$$H_2O_2(\%) = 200\times\frac{\left(\frac{I_r}{N}\right)}{\left(I_d + \frac{I_r}{N}\right)} \quad (4)$$

$$n = 4\times\frac{I_d}{\left(I_d + \frac{I_r}{N}\right)} \quad (5)$$

where I_r is the ring current, I_d is the disk current and N is the ring collection efficiency (here $N = 0.37$).

2.3.2. Zn-air batteries

Rechargeable Zn-air batteries in a two-electrode system were assembled according to the following procedures. The electrolyte used for rechargeable zinc-air batteries was 6 M KOH and 0.2 M $Zn(Ac)_2$ solution; and a polished Zn plate (thickness: 1.0 mm) was used as the anode. The air electrode was prepared by brushing the catalyst onto carbon paper with a loading of 2 mg cm^{-2}. The assembled rechargeable Zn-air batteries were tested at discharge/charge current densities of 10 mA cm^{-2}. The cycling test was performed at ambient temperature by the recurrent galvanic pulse method, in which one cycle consists of one five-minute discharge step and one five-minute charge step.

3. Results and discussion

The synthesis of Fe-N/C catalyst involves two non-solution steps of ball-milling and pyrolysis, as illustrated in Scheme 1. Firstly, a powder mixture containing ZnO, 2-ethylimidazole, Fe-TPP, $(NH_4)_2SO_4$ and trace of DEF were put into the zirconia milling pot, and then were ball-milled using zirconia balls for 2 × 30 min at room temperature to form Fe-TPP ⊂ *rho*-ZIF, a kind of Fe-TPP encapsulated host-guest ZIF complex with the *rho* topology. To remove possible Fe-TPP species adhered to the surface of *rho*-ZIF, the resultant samples were subjected to Soxhlet extraction for 24 h and they still maintained the intrinsic green color from the guest molecule. Since the initial Fe-TPP/ZnO ratios were selected as 1/20, 1/30 and 1/40, the obtained host-guest complexes are denoted as Fe-TPP ⊂ *rho*-ZIF-1/20, Fe-TPP ⊂ *rho*-ZIF-1/30 and Fe-TPP ⊂ *rho*-ZIF-1/40, respectively.

Fig. 1a shows powder X-ray diffraction (XRD) patterns of all the as-obtained hybrid complexes. It can be seen that all the samples have identical powder XRD peaks that match well with those of the simulated *rho*-ZIF [62,63] and no diffraction peaks of the aggregated Fe-TPP crystals were observed, preliminarily judging that Fe-TPP has been encapsulated into *rho*-ZIF. To further confirm this fact, N_2 adsorption–desorption measurements were performed (Fig. 1b). As a typical feature of MOFs, *rho*-ZIF has abundant porous texture and large surface area. If Fe-TPP molecules occupy some cavities of *rho*-ZIF, the BET surface area of *rho*-ZIF inevitable decreases. As expected, the surface areas of the hybrid complexes decrease to 763.5 for Fe-TPP ⊂ *rho*-ZIF-1/20, 982.1 for Fe-TPP ⊂ *rho*-ZIF-1/30 and 1057.6 m^2 g^{-1} for Fe-TPP ⊂ *rho*-ZIF-1/40 from 1113.8 m^2 g^{-1} of the pristine *rho*-ZIF. Meanwhile, a moderate decrease of the pore width for Fe-TPP ⊂ *rho*-ZIF-1/30 was observed compared with that for the pristine *rho*-ZIF (Fig. S1), further proving the incorporation of Fe-TPP molecules into the cavities of *rho*-ZIF. Besides, we also detected the existence of Fe-TPP molecules in Fe-TPP ⊂ *rho*-ZIF by UV–vis absorbance measurements since the Fe-TPP molecules have a characteristic main peak at 412 nm (black curve in Fig. 1c). Taking Fe-TPP ⊂ *rho*-ZIF-1/30 as an example, when it was immersed into chloroform solution for 4 h, the filtrate is almost colorless and did not exhibit any obvious UV–vis absorbance (blue curve in Fig. 1c and Fig. 1d). Nevertheless, after several drops of acetic acid were added in this chloroform solution to destroy the structure of *rho*-ZIF, the colorless filtrate became dark green immediately due to the release of Fe-TPP from Fe-TPP ⊂ *rho*-ZIF and the characteristic absorption of Fe-

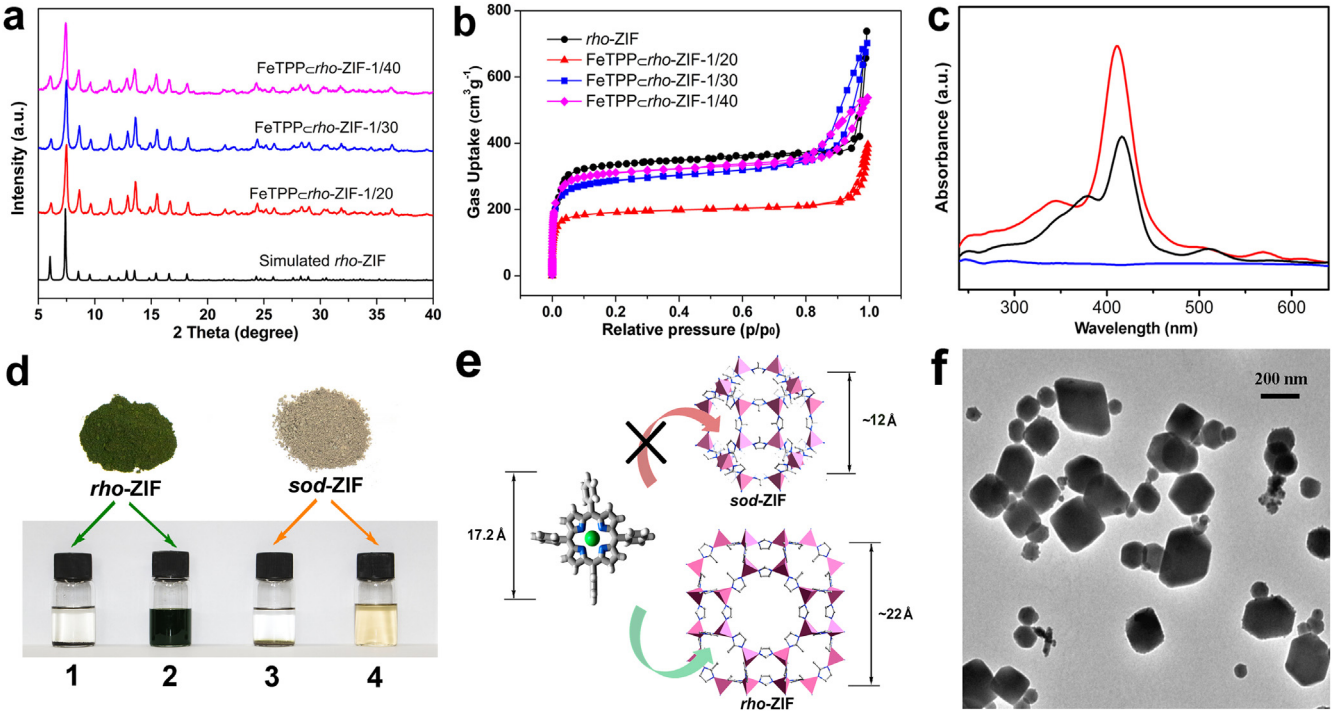

Fig. 1. (a) Powder XRD patterns of the series of FeTPP⊂*rho*-ZIF. (b) N_2 adsorption–desorption isotherms of pristine *rho*-ZIF and the series of Fe-TPP⊂*rho*-ZIF. (c) UV–vis spectra in chloroform solution: Fe-TPP solution (black line), filtrate of Fe-TPP⊂*rho*-ZIF-1/30 (blue line) and filtrate of Fe-TPP⊂*rho*-ZIF-1/30 after adding acetic acid (red line). (d) Washed samples of Fe-TPP⊂*rho*-ZIF-1/30 (**1**: in chloroform solution; **2**: in chloroform solution with the addition of acetic acid) and Fe-TPP/*sod*-ZIF (**3**: in chloroform solution; **4**: in chloroform solution with the addition of acetic acid). (e) Fe-TPP molecule, *sod*- and *rho*-ZIF cages from single-crystal XRD structure with ZnN_4 pink tetrahedra (double-sided arrows indicate their sizes). (f) TEM image of FeTPP⊂*rho*-ZIF-1/30.

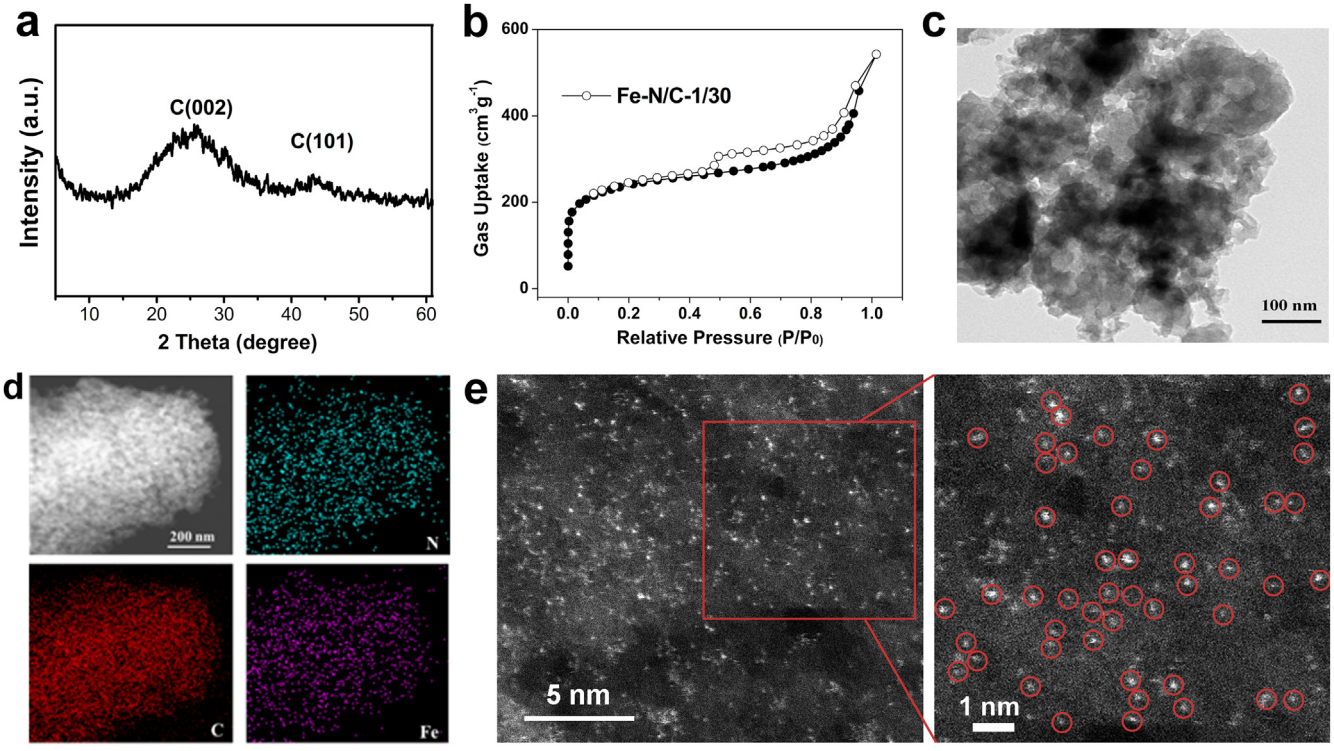

Fig. 2. (a) Powder XRD pattern of Fe-N/C-1/30. (b) N_2 adsorption/desorption isotherms of Fe-N/C-1/30. (c) TEM image, (d) STEM image and corresponding elemental mappings of Fe-N/C-1/30. (e) HAADF-STEM image and enlarged image of Fe-N/C-1/30. Atomically dispersed Fe centers are highlighted by red circles.

TPP appeared accordingly (red curve in Fig. 1c and Fig. 1d). Thus, all above results suggest that the Fe-TPP molecules are successfully encapsulated in *rho*-ZIF. To further clarify the feasibility of the encapsulation process at the molecular level, the commonly used *sod*-type ZIF-8 was synthesized under the similar conditions by using 2-methylimidazole as the linker instead of 2-ethylimidazole to encage Fe-

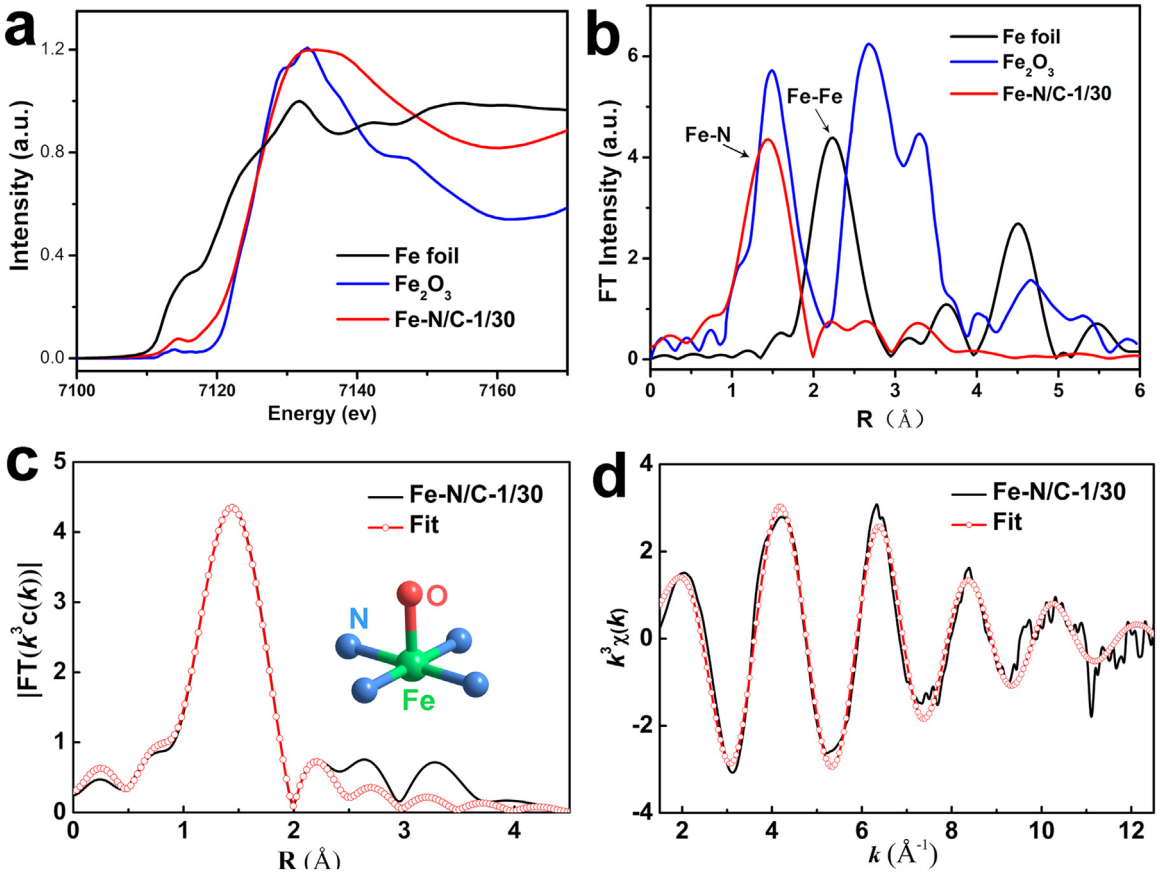

Fig. 3. (a) Fe K-edge XANES spectra and (b) Fourier-transformed EXAFS of Fe-N/C-1/30 with references. Fitting curves of the EXAFS of Fe-N/C-1/30 in r-space (c) and k-space (d).

TPP molecules. As expected, the Fe-TPP species were only physically mixed in the as-synthesized *sod*-type ZIF-8 sample and they can be thoroughly removed by a simple washing procedure, only leaving the yellowish pristine ZIF-8 solids (Fig. 1d and Fig. S2). This phenomenon can be explained by the fact that the relatively small interior cage of *sod*-type ZIF (~ 12 Å) [43] cannot accommodate large Fe-TPP molecule (~ 17.2 Å), whereas ZIFs with *rho* topology have larger cavities (~ 22 Å) that match well with the Fe-TPP molecule [60,61] (Fig. 1e). These experimental and analytical results not only demonstrate that the original ordered and porous structure of *rho*-ZIF remains unchanged after host-guest hybridization, but also further confirm that Fe-TPP molecules indeed occupy the interior cages of *rho*-ZIF. The occupancies of the Fe-TPP molecule in each cage of *rho*-ZIF determined by inductively coupled plasma atomic emission spectroscopy (ICP-AES) tests, are 0.82 for Fe-TPP⊂*rho*-ZIF-1/20, 0.61 for Fe-TPP⊂*rho*-ZIF-1/30, and 0.54 for Fe-TPP⊂*rho*-ZIF-1/40, respectively, which fit well with the change trend of BET values discussed above. Although the Fe-TPP⊂*rho*-ZIF complexes were prepared in a mechanochemical method, the obtained materials still showed relatively regular polyhedron morphology (Fig. 1f and Fig. S3). More importantly, the mechanochemical synthesis of the host-guest Fe-TPP⊂*rho*-ZIF complexes needs only traces of organic liquid, tens of minutes, room temperature and small reaction space, and therefore it is demonstrated to be a facile, highly efficient and scalable fabrication process.

As a representative example, Fe-TPP⊂*rho*-ZIF-1/30, synthesized with the initial Fe-TPP/ZnO molar ratio of 1/30, was transformed into N-doped porous carbon (Fe-N/C-1/30) by pyrolysis at 950 °C under N_2 atmosphere. Other samples obtained at different pyrolysis temperatures also with Fe-TPP⊂*rho*-ZIF-1/30 as the precursor have similar XRD pattern with Fe-N/C-1/30 (Fig. S4). The XRD pattern of Fe-N/C-1/30 in Fig. 2a shows two broad diffraction peaks centered at 25.3° and 43.7°, which are related to the partially graphitic carbon, and no characteristic peaks of Zn species and aggregated Fe-containing species appear. The presence of graphitized carbon has been further confirmed by Raman spectrum (Fig. S5). At such a high pyrolysis temperature (950 °C), the *in-situ* formed Zn species from ZIFs have sublimed, which has been well demonstrated in many literatures [53–58]. The as-prepared Fe-N/C-1/30 inherits highly porous structure of the precursor with BET surface area as high as 1009 m^2 g^{-1} (Fig. 2b), which can be partially attributed to the sublimation of the *in-situ* formed Zn species during the pyrolyzation of ZIFs. The gradual increase of the BET surface area for the samples (Fe-N/C-1/20, Fe-N/C-1/30, and Fe-N/C-1/40) further confirms that the *in-situ* formed Zn species act as the pore-forming agent (Fig. S6). Moreover, ICP-AES demonstrated that the iron loading of Fe-N/C-1/30 was up to 3.8 wt%. The combination of high iron loading and abundant porosity is favorable for exposing numerous Fe-N active moieties that are essential for the high activity of Fe-N/C as the ORR catalyst. It should be noted that neither assistant reagents nor post-ammonia and -acid treatments were used in preparing Fe-N/C, which demonstrates that our method is a facile and environmentally friendly fabrication process.

The morphology and microstructure of Fe-N/C-1/30 were characterized by electron microscopy techniques. In good agreement with the XRD results, no visible iron-containing species in the form of particles or other shapes were observed in TEM image (Fig. 2c). Meanwhile, the elemental mapping images (Fig. 2d) indicate that C, N and Fe elements are uniformly distributed over the entire particles. These observations imply that numerous iron moieties may be highly dispersed in the form of tiny clusters or single atoms. Furthermore, the aberration-corrected high angle annular dark-field scanning transmission electron microscope (HAADF-STEM) image at an atomic resolution presented in Fig. 2e shows a large number of bright dots on the carbon

matrix (highlighted by red circles), clearly indicating the existence of densely and atomically dispersed Fe species. Additional HAADF-STEM images (Fig. S7) of Fe-N/C-1/30 at different regions further prove the fairly homogeneous dispersion of the Fe atoms and almost no clusters or small particles are observed in the vicinity of the single atoms.

The local and electronic structures of Fe-N/C-1/30 in atomic level were further investigated by X-ray absorption near-edge structure (XANES) and extended X-ray absorption fine structure (EXAFS). As shown in Fig. 3a, the XANES curve discloses that the near-edge absorption energy of Fe-N/C-1/30 locates between those of Fe_2O_3 and Fe foil, implying that the valence state of the atomically dispersed Fe moieties is between 3 and 0. Meanwhile, the pre-edge peak at ~ 7115 eV for Fe-N/C-1/30, which is different from those of Fe foil and Fe_2O_3 in intensity, shape, and position, can be assigned to Fe 1s→3d transition, a quadruple allowed transition, and it has been considered as a possible fingerprint of the Fe-N_4 square-planar structure [31,64]. The EXAFS curve for Fe-N/C-1/30 presents a primary peak located at ~ 1.5 Å, which corresponds to the Fe–N(O) scattering path, and no obvious Fe-Fe peak (~ 2.25 Å) was detected (Fig. 3b), indicating that the Fe species are atomically dispersed in the as-obtained product. A least-squares fitting was carried out to further obtain quantitative structural parameters of Fe in Fe-N/C-1/30, such as the fitting parameters (Table 1) and the fitting curves in r-space (Fig. 3c) and k-space (Fig. 3d). The coordination number of Fe was about 5 and the mean bond length was *ca.* 2.0 Å. On the basis of the above analysis, the local atomic structure around Fe was constructed, and it indicates that the isolated Fe atom was four-fold coordinated by N atoms and one O_2 molecule might be adsorbed on the Fe atom in perpendicular to Fe-N_4 plane as shown in the inset of Fig. 3c.

The chemical states of elements in Fe-N/C-1/30 sample were also examined with X-ray photoelectron spectroscopy (XPS). The survey XPS spectrum for Fe-N/C-1/30 confirms the presence of Fe, C, N, and O elements (Fig. S8a). The high-resolution Fe 2p spectrum exhibits an evident signal at around 711.0 eV, which can be assigned to the Fe species of Fe–N_x configuration (Fig. S8b) [65,66]. For comparison, a control sample (denoted as Fe-N/C-mix) was prepared by physically mixing pristine *rho*-ZIF with Fe-TPP as the precursor while keeping other conditions constant (see Experimental Section for details). The high-resolution N1s spectrum for Fe-N/C materials can be divided into several characteristic peaks at 398.4, 399.0, 399.8, 401.1 and 402.8 eV (Fig. S9), which are assigned to pyridinic-N, Fe-N, pyrrolic-N, graphitic-N, and oxidized-N, respectively [55,57]. Furthermore, according to the XPS results, the total Fe content and the proportion of nitrogen coordinated with Fe (Fe-N_4) on Fe-N/C-1/30 surface were much higher than those on Fe-N/C-mix surface (Fig. S9 and Table S1), which demonstrates that Fe-N/C-1/30 possesses more isolated Fe-N_4 sites compared with Fe-N/C-mix. This is probably attributed to the host-guest confinement effect of Fe-TPP ⊂ *rho*-ZIF precursor that prevents the loss of Fe moieties during the pyrolysis process, which is in sharp contrast to the physically mixed precursor.

The ORR activity of the catalysts was firstly investigated in O_2-saturated 0.1 M KOH with rotating disk electrode (RDE) technique at 1600 rpm with a scan rate of 10 mV s^{-1}. The linear sweep voltammetry (LSV) polarization curves show that Fe-N/C-1/30 possesses the best activity in term of the most positive onset (E_{onset}) and halfwave potential ($E_{1/2}$). As shown in Fig. 4a, E_{onset} of Fe-N/C-1/30 is 1.04 V, very close to that of commercial Pt/C (1.02 V), and $E_{1/2}$ of Fe-N/C-1/30 reaches 0.895 V, even ~ 50 mV more positive than that on commercial Pt/C (0.845 V). Fe-N/C-1/20 and Fe-N/C-1/40 have almost similar activity with Fe-N/C-1/30 in KOH (Fig. S10). As a reference, Fe-N/C-mix catalyst exhibits poor E_{onset} of 0.97 V and $E_{1/2}$ of 0.802 V, indicating the critical role of host-guest confinement effect for immobilizing iron centers and enhancing ORR performance. Excitingly, Fe-N/C-1/30 also exhibits good ORR activity in 0.5 M H_2SO_4 solution (Fig. S11). Furthermore, the ORR kinetics of the catalysts were studied by RDE at rotating speeds from 625 to 2500 rpm (Fig. 4b). It can be clearly observed that the current density of Fe-N/C-1/30 also increases accordingly with increasing the rotating speed, which is attributed to the enhanced diffusion rate at high speeds. The Koutechy-Levich (K-L) plots of Fe-N/C-1/30 were obtained from LSVs with the potentials ranging from 0.73 to 0.6 V *vs.* RHE, as shown in Fig. 4c. All the K-L plots present good linearity at all the applied potentials, which indicates first-order reaction kinetics with respect to the O_2 concentration. Based on the K-L equation, the electron–transfer number (n) was calculated to be ~ 3.92, very close to the ideal value of 4.0 for Pt/C. The formation of peroxide species (HO_2^-) on Fe-N/C-1/30 during the ORR was further monitored by rotating ring-disk electrode (RRDE) measurements. Based on the recorded data of ring and disk current, the yield of HO_2^- is below 7.5% in the whole potential range, while the n value of electron-transfer number is ~ 4.0 (Fig. S12 and Fig. S13). This is consistent with the result obtained from the K-L plots, suggesting the ORR process catalyzed on Fe-N/C-1/30 follows the four electron pathway ideally.

The long-term durability of catalysts was assessed by chronoamperometric measurement in O_2-saturated 0.1 M KOH solution at a rotation speed of 1600 rpm and the applied potential of 0.75 V (Fig. 4d). After 30000 s reaction, the as-prepared Fe-N/C-1/30 exhibits a good durability with 94.8% of the original current density maintained, significantly higher than 83.6% for the commercial Pt/C catalyst, which demonstrates a negligible degradation of surface active sites on Fe-N/C-1/30. The stability of Fe-N/C-1/30 was also evaluated by cycling the catalyst between 0.6 and 1.0 V at a sweep rate of 50 mV s^{-1} in O_2-saturated 0.1 M KOH and 0.5 M H_2SO_4 solution, respectively. After 10000 continuous cycles (Fig. 4e and f), the LSV curve of Fe-N/C-1/30 shows a negligible decrease of $E_{1/2}$, showing the outstanding durability of Fe-N/C-1/30 in both alkaline and acid solutions (Fig. S14).

To examine the fuel crossover effect, methanol tolerance was investigated by instantaneously adding 3 M methanol during the durability measurement of Fe-N/C-1/30 and Pt/C. After the addition of methanol, there was little crossover effect that can be observed from the CV curve on Fe-N/C, implying the inactivity of Fe-N/C-1/30 toward methanol oxidation (Fig. 5a). However, for the CV curve of Pt/C, the ORR peak vanishes and the typical oxidation peak of methanol appears after the introduction of methanol (Fig. S15). The above results demonstrate that Fe-N/C-1/30 has good tolerance to methanol crossover. In addition, it is well known that SCN^- ion has a high affinity to iron centers and can poison isolated Fe-N_4 sites in electrocatalytic process [66–68]. As shown in Fig. 5b, the $E_{1/2}$ of Fe-N/C-1/30 decreases significantly by about 130 mV after the addition of 0.01 M NaSCN into O_2-saturated 0.5 M H_2SO_4. When the electrode was rinsed with deionized water and then re-evaluated in 0.1 M KOH solution, the ORR polarization curve gradually positively shifted and finally recovered to the original level (Fig. 5c). This phenomenon is attributed to the recovery of Fe-N_4 sites, since the dissociation of SCN^- adsorped on the surface of Fe-N/C-1/30 occurs in alkaline solution (Fig. S16). Based on the above results, it can be deduced that the excellent ORR activity of Fe-N/C-1/30 originates from the isolated Fe-N_4 moieties.

The oxygen evolution reaction (OER) activity and stability of Fe-N/C-1/30 were also evaluated in O_2-saturated 1 M KOH solution (Fig. S17). Despite only moderate activity, Fe-N/C-1/30 shows a good stability at the current density of 10 mA cm^{-2} for ~ 12 h. Encouraged by the outstanding ORR half-cell performance and good OER stability,

Table 1
Fe K-edge EXAFS curve fitting parameters of Fe-N/C-1/30[a].

Sample	Path	*N*	*R* (Å)	σ^2 (× 10^{-3} Å^2)	ΔE_0 (eV)	*R*, %
Fe-N/C-1/30	Fe-N(O)	5.0 ± 0.4	1.99 ± 0.02	9.4 ± 2	3.7 ± 2	0.005

[a] N is coordination number, R is the distance between absorber and backscatter atoms, σ^2 is Debye-Waller factor, ΔE_0 is inner potential correction; *R* factor indicates the goodness of the fit.

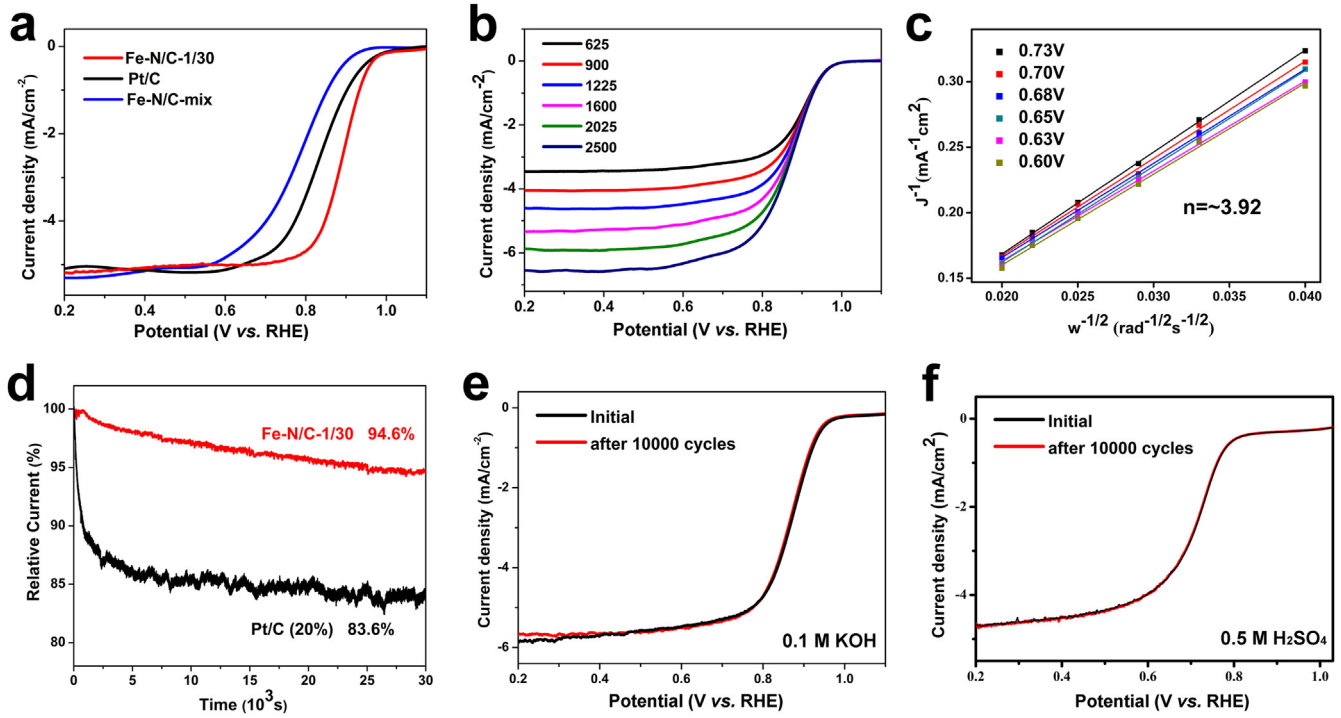

Fig. 4. (a) LSV curves of ORR on Fe-N/C-1/30, Fe-N/C-mix and Pt/C at 1600 rpm with a scan rate of 10 mV s^{-1}. (b) LSV curves of Fe-N/C-1/30 at various rotation rates. (c) K-L plots at different electrode potentials of Fe-N/C-1/30. (d) Normalized current-time (i–t) chronoamperometric responses of Fe-N/C-1/30 and Pt/C (20%) at 0.75 V for 30,000 s in O_2 saturated 0.1 M KOH solution at a rotation rate of 1600 rpm. ORR polarization curves before and after 10k potential cycles at a scan rate of 50 mV s^{-1} in O_2 saturated 0.1 M KOH solution (e) and 0.5 M H_2SO_4 solution (f).

rechargeable zinc-air batteries were assembled using the as-prepared Fe-N/C-1/30 catalyst as the active air-electrode material. An open circuit potential of 1.525 V is detected for the Fe-N/C-based zinc-air battery, suggesting Fe-N/C-1/30 performs as a good electrocatalyst under practical conditions (Fig. S18). As shown in Fig. 5d, the maximum power density of the Fe-N/C-1/30-based zinc-air battery is determined to be 121.8 mW cm^{-2}, which is comparable to that of the Pt/C-based counterpart (~ 132 mW cm^{-2}). Typical galvanostatic discharge curves in Fig. 5e illustrate the voltage of 1.40 V at current density of 2 mA cm^{-2} and 1.32 V at 5 mA cm^{-2} for 2 h, showing little voltage decay during the

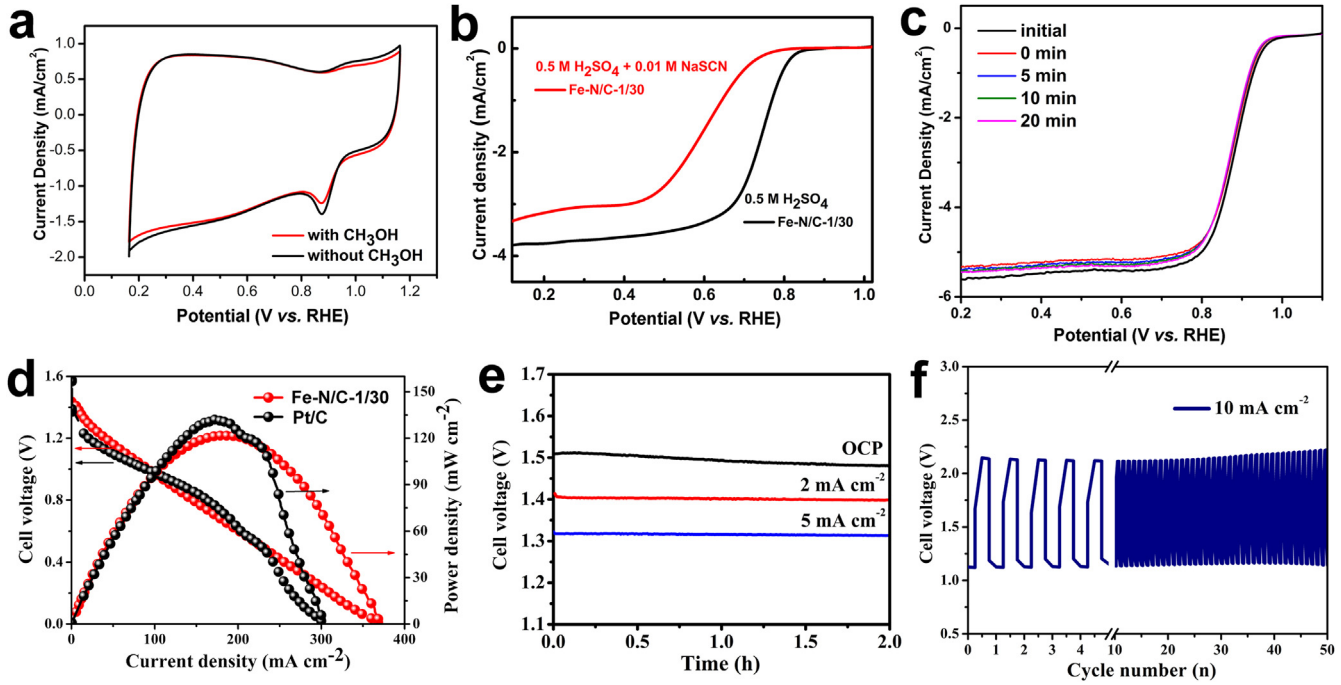

Fig. 5. (a) CVs of Fe-N/C-1/30 in O_2-saturated 0.1 M KOH without and with 3 M methanol. ORR polarization curves of (b) Fe-N/C-1/30 before and after the addition of 0.01 M NaSCN in 0.5 M H_2SO_4 at 1600 rpm with a scan rate of 10 mV s^{-1}, and (c) SCN^- poisoned Fe-N/C-1/30 in 0.1 M KOH. Characteristics of Fe-N/C-1/30 electrocatalyst based Zn-air batteries (catalyst loading: 2.0 mg cm^{-2}; anode: zinc foil): (d) Polarization and power density curves of the Zn-air batteries with different catalysts. (e) Galvanostatic discharge curves. (f) Galvanostatic discharge-charge cycling curves at 10 mA cm^{-2} of Zn-air batteries with the Fe-N/C-1/30 as catalyst.

test. Moreover, cycle performance of the assembled battery has also been evaluated and it only exhibits a slight performance decay with a small increase in the potential gap by 0.063 V after 50 cycles (Fig. 5f).

Instead of Fe-TPP, simple iron salts such as ferrous oxalate and ferric acetylacetonate were also used as iron sources to prepare Fe-N/C materials by this non-solution method. Unfortunately, Fe centers were seriously aggregated and the obtained Fe-N/C materials showed very poor electrochemical activity (Fig. S19). Thus, the macrocyclic structure of Fe-TTP molecules guarantees the isolation of the atomic Fe moieties during the pyrolysis process, preventing the formation of Fe-containing particles. Besides, initial Fe-TPP/ZnO molar ratios from 1/20 to 1/40 for synthesizing Fe-N/C were also investigated by a series of characterizations and measurements. TEM image of Fe-N/C-1/20 shows that some aggregated particles can be observed (Fig. S20), in contrast with that of Fe-N/C-1/30. Despite different BET surface areas, three Fe-N/C catalysts all show high ORR activity (Fig. S10), which is in accordance with their high iron loadings (4.1 wt% for Fe-N/C-1/20, 3.8 wt% for Fe-N/C-1/30 and 3.2 wt% for Fe-N/C-1/40). This result implies that abundant active sites play a crucial role in the ORR catalysis process in this system.

4. Conclusion

By one-pot mechanochemical method, Fe-TPP molecules can be encapsulated into the large interior cages of *rho*-ZIF to form host-guest Fe-TPP ⊂ *rho*-ZIF complexes with high yield. As precursors, Fe-TPP ⊂ ZIF complexes were then pyrolyzed into Fe-N/C catalysts with no need of solvent washing, post-ammonia and -acid treatments, which greatly simplified the preparation procedures. Owing to the host-guest confinement effect, Fe centers are effectively isolated during pyrolysis and atomically dispersed in form of Fe-N_4 active sites on the carbon matrice, which was confirmed by electron microscope and X-ray absorption fine structure techniques. Moreover, the catalyst showed excellent ORR activity, good methanol tolerance and high durability. Our work may provide an insight into the facile and large-scale production of high-performance and stable non-precious metal catalysts with atomic-level dispersion.

Acknowledgements

This work was supported by National Natural Science Foundation of China (11474204, 21601014, 21471016, 51761145046) and the 111 Project (B07012).

Appendix A. Supporting information

Supplementary data associated with this article can be found in the online version at doi:10.1016/j.nanoen.2018.07.033.

References

[1] Y. Nie, L. Li, Z. Wei, Chem. Soc. Rev. 44 (2015) 2168–2201.
[2] Y. Jiao, Y. Zheng, M. Jaroniec, S.Z. Qiao, Chem. Soc. Rev. 44 (2015) 2060–2086.
[3] W. Xia, A. Mahmood, Z. Liang, R. Zou, S. Guo, Angew. Chem. Int. Ed. 55 (2016) 2650–2676.
[4] J. Pan, Y.Y. Xu, H. Yang, Z. Dong, H. Liu, B.Y. Xia, Adv. Sci. 5 (2018) 1700691.
[5] Z. Pei, H. Li, Y. Huang, Q. Xue, Y. Huang, M. Zhu, Z. Wang, C. Zhi, Energy Environ. Sci. 10 (2017) 742–749.
[6] Z. Pei, Z. Tang, Z. Liu, Y. Huang, Y. Wang, H. Li, Q. Xue, M. Zhu, D. Tang, C. Zhi, J. Mater. Chem. A 6 (2018) 489–497.
[7] B.Y. Xia, Y. Yan, N. Li, H.B. Wu, X.W. Lou, X. Wang, Nat. Energy 1 (2016) 15006.
[8] J.C. Meier, I. Katsounaros, C. Galeano, H.J. Bongard, A.A. Topalov, A. Kostka, A. Karschin, F. Schüth, K.J.J. Mayrhofer, Energy Environ. Sci. 5 (2012) 9319–9330.
[9] X.L. Tian, Y.Y. Xu, W. Zhang, T. Wu, B.Y. Xia, X. Wang, ACS Energy Lett. 2 (2017) 2035–2043.
[10] Q. Wang, Z.Y. Zhou, Y.J. Lai, Y. You, J.G. Liu, X.L. Wu, E. Terefe, C. Chen, L. Song, M. Rauf, N. Tian, S.G. Sun, J. Am. Chem. Soc. 136 (2014) 10882–10885.
[11] H. Chung, D. Cullen, D. Higgins, B. Sneed, E. Holby, K. More, P. Zelenay, Science 357 (2017) 479–484.
[12] A. Zitolo, V. Goellner, V. Armel, M. Sougrati, T. Mineva, L. Stievano, E. Fonda, F. Jaouen, Nat. Mater. 14 (2015) 937–942.
[13] L. Ma, S. Chen, Z. Pei, Y. Huang, G. Liang, F. Mo, Q. Yang, J. Su, Y. Gao, J.A. Zapien, C. Zhi, ACS Nano 12 (2018) 1949–1958.
[14] F. Jaouen, J. Herranz, M. Lefèvre, J.-P. Dodelet, U.I. Kramm, I. Herrmann, P. Bogdanoff, J. Maruyama, T. Nagaoka, A. Garsuch, J.R. Dahn, T. Olson, S. Pylypenko, P. Atanassov, E.A. Ustinov, ACS Appl. Mater. Interfaces 1 (2009) 1623–1639.
[15] M. Lefèvre, E. Proietti, F. Jaouen, J.-P. Dodelet, Science 324 (2009) 71–74.
[16] G. Wu, K.L. More, C.M. Johnston, P. Zelenay, Science 332 (2011) 443–447.
[17] Z.Y. Wu, X.X. Xu, B.C. Hu, H.W. Liang, Y. Lin, L.F. Chen, S.H. Yu, Angew. Chem. Int. Ed. 54 (2015) 8179–8183.
[18] S.H. Ahn, X. Yu, A. Manthiram, Adv. Mater. 29 (2017) 1606534.
[19] M. Ferrandon, A.J. Kropf, D.J. Myers, K. Artyushkova, U. Kramm, P. Bogdanoff, G. Wu, C.M. Johnston, P. Zelenay, J. Phys. Chem. C. 116 (2012) 16001–16013.
[20] W. Liu, L. Zhang, X. Liu, X. Liu, X. Yang, S. Miao, W. Wang, A. Wang, T. Zhang, J. Am. Chem. Soc. 139 (2017) 10790–10798.
[21] J.-D. Yi, R. Xu, Q. Wu, T. Zhang, K.-T. Zang, J. Luo, Y.-L. Liang, Y.-B. Huang, R. Cao, ACS Energy Lett. 3 (2018) 883–889.
[22] H. Fei, J. Dong, Y. Feng, C.S. Allen, C. Wan, B. Volosskiy, M. Li, Z. Zhao, Y. Wang, H. Sun, Nat. Catal. 1 (2018) 63–72.
[23] X. Fang, Q. Shang, Y. Wang, L. Jiao, T. Yao, Y. Li, Q. Zhang, Y. Luo, H. Jiang, Adv. Mater. 30 (2018) 1705112.
[24] J. Thomas, Nature 525 (2015) 325.
[25] X.F. Yang, A. Wang, B. Qiao, J. Li, J. Liu, T. Zhang, Acc. Chem. Res. 46 (2013) 1740–1748.
[26] J. Liu, ACS Catal. 7 (2017) 34–59.
[27] C. Zhu, S. Fu, Q. Shi, D. Du, Y. Lin, Angew. Chem. Int. Ed. 56 (2017) 13944–13960.
[28] E. Proietti, F. Jaouen, M. Lefèvre, N. Larouche, J. Tian, J. Herranz, J.-P. Dodelet, Nat. Commun. 2 (2011) 416.
[29] C. Zhang, Y.C. Wang, B. An, R. Huang, C. Wang, Z. Zhou, W. Lin, Adv. Mater. 29 (2017) 1604556.
[30] X.J. Wang, H.G. Zhang, H.H. Lin, S. Gupta, C. Wang, Z.X. Tao, H. Fu, T. Wang, J. Zheng, G. Wu, X.G. Li, Nano Energy 25 (2016) 110–119.
[31] Q. Liu, X. Liu, L. Zheng, J. Shui, Angew. Chem. Int. Ed. 57 (2018) 1204–1208.
[32] J. Shui, C. Chen, L. Grabstanowicz, D. Zhao, D.-J. Liu, Proc. Natl. Acad. Sci. USA 112 (2015) 10629–10634.
[33] D. Zhao, J.L. Shui, L.R. Grabstanowicz, C. Chen, S.M. Commet, T. Xu, J. Lu, D.J. Liu, Adv. Mater. 26 (2014) 1093–1097.
[34] J. Li, Y. Song, G. Zhang, H. Liu, Y. Wang, S. Sun, X. Guo, Adv. Funct. Mater. 27 (2017) 1604356.
[35] H. Meng, N. Larouche, M. Lefèvre, F. Jaouen, B. Stansfield, J.-P. Dodelet, Electrochim. Acta 55 (2010) 6450–6461.
[36] H. Shen, E. Gracia-Espino, J. Ma, H. Tang, X. Mamat, T. Wagberg, G. Hu, S. Guo, Nano Energy 35 (2017) 9–16.
[37] S.L. James, C.J. Adams, C. Bolm, D. Braga, P. Collier, T. Friščić, F.K. Grepioni, G. Hyett, W. Jones, A. Krebs, J. Mack, L. Maini, A.G. Orpen, I.P. Parkin, W.C. Shearouse, J.W. Steed, D.C. Waddell, Chem. Soc. Rev. 41 (2012) 413–447.
[38] P.J. Beldon, L. Fábián, R.S. Stein, A. Thirumurugan, A.K. Cheetham, T. Friščić, Angew. Chem. Int. Ed. 49 (2010) 9640–9643.
[39] T. Friščić, D.G. Reid, I. Halasz, R.S. Stein, R.E. Dinnebier, M.J. Duer, Angew. Chem. Int. Ed. 49 (2010) 712–715.
[40] W.B. Yuan, T. Friščić, D. Apperley, S.L. James, Angew. Chem. Int. Ed. 49 (2010) 3916–3919.
[41] T. Friščić, A.V. Trask, W. Jones, W.D.S. Motherwell, Angew. Chem. Int. Ed. 45 (2006) 7546–7550.
[42] M. Klimakow, P. Klobes, A.F. Thünemann, K. Rademann, F. Emmerling, Chem. Mater. 22 (2010) 5216–5221.
[43] R. Banerjee, A. Phan, B. Wang, C. Knobler, H. Furukawa, M. O'Keeffe, O.M. Yaghi, Science 319 (2008) 939–943.
[44] R. Li, X.Q. Ren, J.S. Zhao, X. Feng, X. Jiang, X.X. Fan, Z.G. Lin, X.G. Li, C.W. Hu, B. Wang, J. Mater. Chem. A 2 (2014) 2168–2173.
[45] R. Li, X.Q. Ren, H.W. Ma, X. Feng, Z.G. Lin, X.G. Li, C.W. Hu, B. Wang, J. Mater. Chem. A 2 (2014) 5724–5729.
[46] X. Zhao, Y. Duan, F. Yang, W. Wei, Y. Xu, C. Hu, Inorg. Chem. 56 (2017) 14506–14512.
[47] J. Sun, H. Yin, P. Liu, Y. Wang, X. Yao, Z. Tang, H. Zhao, Chem. Sci. 7 (2016) 5640–5646.
[48] H. Tang, H. Yin, J. Wang, N. Yang, D. Wang, Z. Tang, Angew. Chem. Int. Ed. 52 (2013) 5585–5589.
[49] W.Y. Gao, M. Chrzanowski, S. Ma, Chem. Soc. Rev. 43 (2014) 5841–5866.
[50] W. Li, J. Wu, D.C. Higgins, J.Y. Choi, Z. Chen, ACS Catal. 2 (2012) 2761–2768.
[51] H. Schulenburg, S. Stankov, V. Schünemann, J. Radnik, I. Dorbandt, S. Fiechter, P. Bogdanoff, H. Tributsch, J. Phys. Chem. B 107 (2003) 9034–9041.
[52] S. Maldonado, K.J. Stevenson, J. Phys. Chem. B 108 (2004) 11375–11383.
[53] Y. Chen, S. Ji, Y. Wang, J. Dong, W. Chen, Z. Li, R. Shen, L. Zheng, Z. Zhuang, D. Wang, Y. Li, Angew. Chem. Int. Ed. 56 (2017) 6937–6941.
[54] P. Yin, T. Yao, Y. Wu, L. Zheng, Y. Lin, W. Liu, H. Ju, J. Zhu, X. Hong, Z. Deng, G. Zhou, S. Wei, Y. Li, Angew. Chem. Int. Ed. 55 (2016) 10800–10805.
[55] Q. Lai, L. Zheng, Y. Liang, J. He, J. Zhao, J. Chen, ACS Catal. 7 (2017) 1655–1663.
[56] R. Zheng, S. Liao, S. Hou, X. Qiao, G. Wang, L. Liu, T. Shu, L. Du, J. Mater. Chem. A 4 (2016) 7859–7868.
[57] H. Zhang, S. Hwang, M. Wang, Z. Feng, S. Karakalos, L. Luo, Z. Qiao, X. Xie, C. Wang, D. Su, Y. Shao, G. Wu, J. Am. Chem. Soc. 139 (2017) 14143–14149.
[58] V. Armel, S. Hindocha, F. Salles, S. Bennett, D. Jones, F. Jaouen, J. Am. Chem. Soc. 139 (2017) 453–464.
[59] J. Wang, G. Han, L. Wang, L. Du, G. Chen, Y. Gao, Y. Ma, C. Du, X. Cheng, P. Zuo,

G. Yin, Small 14 (2018) 1704282.
[60] S. Fu, C. Zhu, D. Su, J. Song, S. Yao, S. Feng, M.H. Engelhard, D. Du, Y. Lin, Samll 14 (2018) 1703118.
[61] M. Newville, J. Synchrotron Radiat. 8 (2001) 96–100.
[62] C.T. He, L. Jiang, Z.M. Ye, R. Krishna, Z.S. Zhong, P.Q. Liao, J.Q. Xu, G. Ouyang, J.P. Zhang, X.M. Chen, J. Am. Chem. Soc. 137 (2015) 7217–7223.
[63] X.C. Huang, Y.Y. Lin, J.P. Zhang, X.M. Chen, Angew. Chem. Int. Ed. 45 (2006) 1557–1559.
[64] D. Deng, X. Chen, L. Yu, X. Wu, Q. Liu, Y. Liu, H. Yang, H. Tian, Y. Hu, P. Du, Sci. Adv. 1 (2015) e1500462.
[65] R. Cao, R. Thapa, H. Kim, X. Xu, M.G. Kim, Q. Li, N. Park, M. Liu, J. Cho, Nat. Commun. 4 (2013) 2076.
[66] W.J. Jiang, L. Gu, L. Li, Y. Zhang, X. Zhang, L.J. Zhang, J.Q. Wang, J.S. Hu, Z. Wei, L.J. Wan, J. Am. Chem. Soc. 138 (2016) 3570–3578.
[67] M.S. Thorum, J.M. Hankett, A.A. Gewirth, J. Phys. Chem. Lett. 2 (2011) 295–298.
[68] H. Liang, S. Brüller, R.H. Dong, J. Zhang, X.L. Feng, K. Müllen, Nat. Commun. 6 (2015) 7992.